CODE_BRIGHT
v9

VERIFICATION DOCUMENT

https://deca.upc.edu/en/projects/code_bright

UNIVERSITAT POLITÈCNICA DE CATALUNYA
BARCELONATECH
Department of Civil and Environmental Engineering
Division of Geotechnical Engineering and Geosciences

Barcelona, October 2019

1 INTRODUCTION

The performance and accuracy of CODE-BRIGHT has been carefully tested by carrying out analyses of problems with known analytical solutions. Most of the analysis has been carried out as part of international benchmark exercises in which other computational codes has also been used. In the *validation document* the most relevant references has been compiled.

In this document, verifications examples using the present version of CODE_BRIGHT have been performed in order to check that the program is solving the intended equations. Analyses involving T, H, and M problems in isolated or coupled way are described and the numerical results are compared with known analytical solutions.

The first analysis is the classical problem of one-dimensional consolidation involving a hydro-mechanical coupling. The second analysis is the case of radial heat flow to which only the energy equation is solved. The last analysis is related with the problem of convergence of excavations in salt formations, no thermal or hydraulic coupling were considered in this exercise. For the three analyses, comparisons of calculations with the analytical solutions show a good agreement. Therefore, performance of CODE_BRIGHT will be considered successful.

2 ONE-DIMENSIONAL CONSOLIDATION

Consolidation is a transient process of unsteady flow in which there is coupling between flow and volume changes as the soil gradually adjusts to a new effective stress regime.

The problem of one-dimensional consolidation can be described by the following differential equation for the liquid pressure $p_{l,,}$

$$C_v \frac{\partial^2 p_l}{\partial z^2} = \frac{\partial p_l}{\partial t} \tag{2.1}$$

where, C_v is the coefficient of consolidation which has dimensions of (length^2/time) and is calculated as,

$$C_v = \frac{k_w E_{oed}}{\gamma_w} \qquad E_{oed} = \frac{(1-\nu)E}{(1+\nu)(1-2\nu)} \qquad z = H - y \tag{2.2}$$

The one-dimensional consolidation equation (2.1) is a linear equation, which can be made non-dimensional by writing,

$$P_l = \frac{p_l}{p_{lo}} \qquad Z = \frac{z}{H} \qquad T = \frac{C_v t}{H^2} \tag{2.3}$$

where, p_{lo} is a reference pore liquid pressure, H is a characteristic length, and T emerges as a dimensionless time factor. The equation (2.1) then becomes as (2.4),

$$\frac{\partial^2 P_l}{\partial Z^2} = \frac{\partial P_l}{\partial T} \tag{2.4}$$

The assumptions that underpin this equation are material characteristics: incompressible pore fluid, incompressible soil particles, flow of pore fluid governed by Darcy's law, constant stiffness E_{oed} during the consolidation process; and boundary conditions: one-dimensional deformation and flow.

The analytical solution of the one-dimensional consolidation equation as a function of time and position is written as a general Fourier series as,

$$P_l = \frac{4}{\pi} \sum_{m=0}^{\infty} \left\{ \frac{1}{2m+1} \mathrm{e}^{-\pi^2 (2m+1)^2 \frac{T}{4}} \sin\left[\frac{\pi}{2} (2m+1) Z \right] \right\} \tag{2.5}$$

where m is an integer.

Figure 2.1 shows the geometry and finite element mesh for the simulation of the one-dimensional consolidation problem in a saturated medium. The height of the geometry is 1.0 m. The upper side is allowed to drain while the other sides are kept undrained by imposing impermeable boundary condition. An excess liquid pressure is generated applying an external vertical load of $\Delta\sigma$ = 0.1 MPa to the upper boundary. The dissipation of the excess liquid pressure is monitored at different interval times. Constitutive laws and parameters employed are showed in Table 2.1.

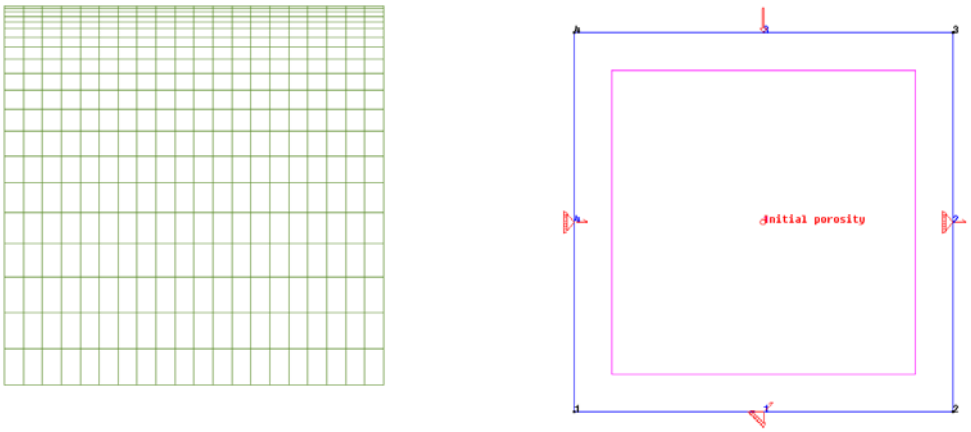

Figure 2.1 Problem geometry, finite element mesh and boundary conditions

MECHANICAL DATA	
Linear elasticity law:	
ITYCL	1
P1: E *(MPa)*	1
P3: ν	0.3
HYDRAULIC DATA	
Intrinsic Permeability:	
ITYCL	1
P1: $(k_{11})_o$ (m^2)	10^{-14}
P2: $(k_{22})_o$ (m^2)	10^{-14}
P3: $(k_{33})_o$ (m^2)	10^{-14}
PHASE PROPERTIES	
Solid phase	
ITYCL	1
P2: ρ_s $(kg\ m^{-3})$	2600
Liquid phase	
ITYCL	1
P1: ρ_{l0} $(kg\ m^{-3})$	1000

Table 2.1 Constitutive laws and parameters for consolidation problem

Figure 2.2 shows the relative excess liquid pressure versus the relative vertical position (or characteristic length), for different time factors. The analytical solution is presented by continues lines. It can be seen that numerical solution is close to the analytical solution.

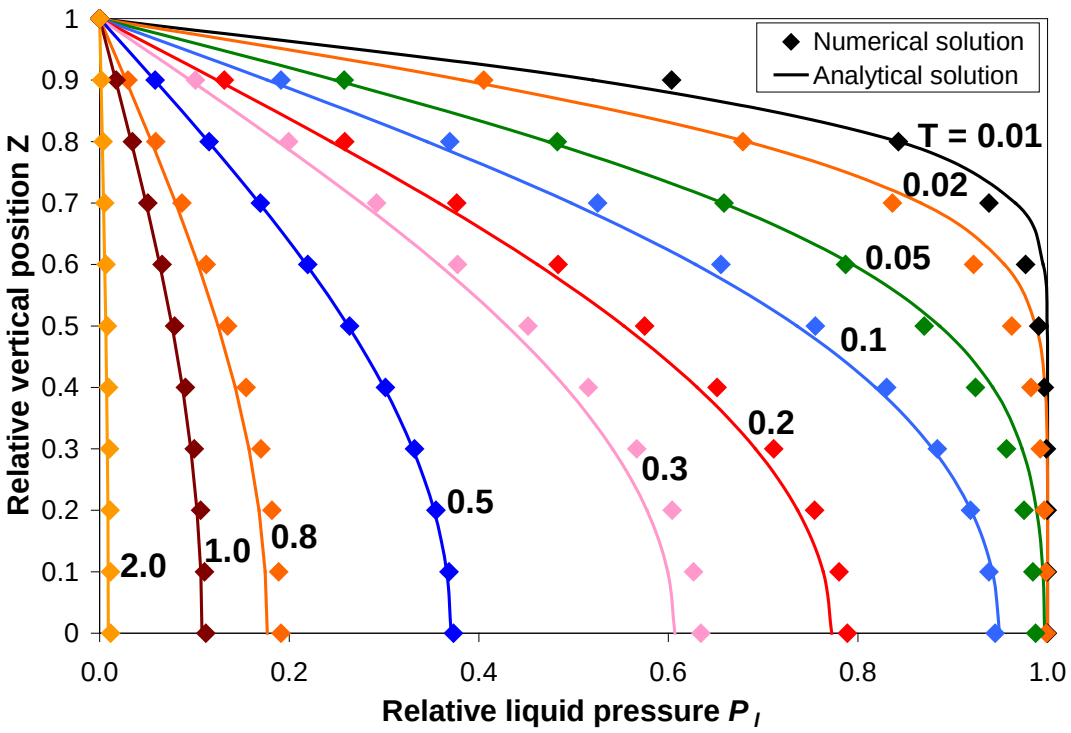

Figure 2.2 Development of liquid pressure as a function of the sample height

Predicted settlement at the surface (top boundary) will be computed as, $\Delta h = \frac{\Delta\sigma}{E_{oed}} H = 0.0743 \text{ m}$. Figure 2.3 shows the contours of vertical displacement obtained in the simulation along the sample height. Figure shows a perfect fit with predicted solution at the surface.

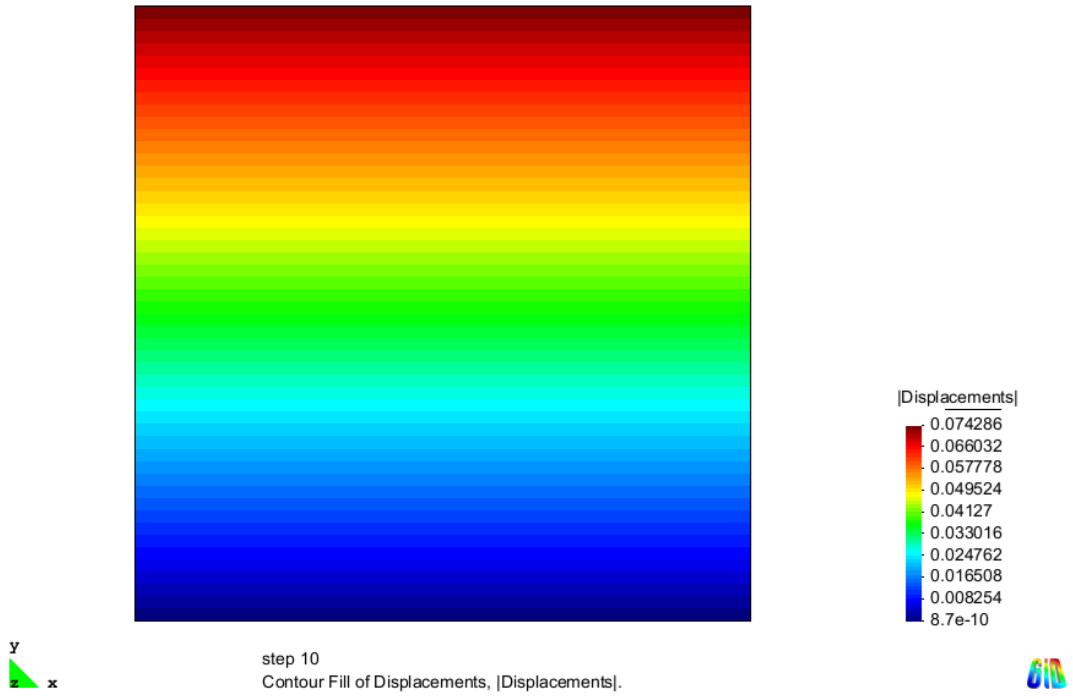

Figure 2.3 Contours of vertical displacement

3 RADIAL HEAT FLOW

The heat flow equation and the confined liquid flow equation are formally identical for the linear case. For this problem, only temperature must be computed and the energy equation becomes,

$$\rho_s c_s \frac{\partial T}{\partial t} + \lambda_s \nabla^2 T = 0 \tag{3.1}$$

where ρ_s is the solid density, C_s is solid specific heat, and λ_s is thermal conductivity. If the parameters are taken constant, the problem is linear. Moreover, if the flow is radial and a source or sink at constant heat rate Q_h is assumed at $r = 0$, then the solution of the problem is given by,

$$T - T_o = \frac{Q_h}{4\pi\lambda_s} W(u); \quad u = \frac{r^2}{4Dt}; \quad D = \frac{\lambda_s}{\rho_s c_s} \tag{3.2}$$

Where, $W(u) = \int_u^\infty \frac{\exp(-y)}{y} dy$ is an integral function, u is dimensionless variable and D is the diffusivity. This is the well-known Theis (1935) solution for radial flow in a confined aquifer.

Radial heat flow problem is simulated both using an axisymmetric geometry and a 3D geometry with an internal radius of r=0.25 m. Constitutive laws and parameters employed in both cases are listed in Table 3.1.

THERMAL DATA	
Conductive flux of heat:	
ITYCL	1
P1: λ_{dry} *(W mK^{-1})*	5.1
P2: λ_{sat} *(W mK^{-1})*	5.1
PHASE PROPERTIES	
Solid phase	
ITYCL	1
P1: C_s *(J kg^{-1}K^{-1})*	874
P2: ρ_s *(kg m^{-3})*	2163

Table 3.1 Constitutive laws and parameters for radial flow problem

3.1 Axisymmetric problem

Figure 3.1, shows the axisymmetric geometry with an internal radius of r=0.25 m. Different values for the external radius (b) were studied (b = 10, 30, 50 and 100 m), to analyse the influence of the position of boundary condition on the results. An initial temperature of T_o=40ºC is imposed at the right boundary and a constant heat flow of Q_h=930 J/s/m (this is the power of one meter of canister) is imposed at the left boundary. For the geometry adopted, prescribed heat flow per square meter is equal to $Q_{h\ applied} = Q_h / 2\pi r h = 592\ \mathrm{J/s/m^2}$, where h is the height of the model (h=10m). This is the value imposed in the line that represents the cylindrical internal surface.

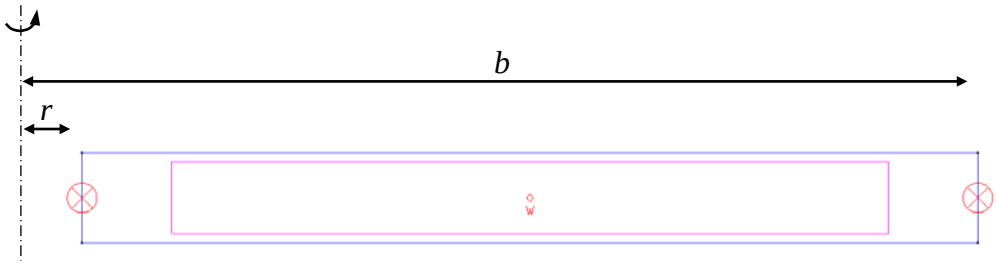

Figure 3.1 Problem geometry and boundary conditions (Axisymmetric geometry)

Figure 3.2 shows the resulting variation of temperature in time for four different finite element geometries varying the position of the boundary condition away of the heat source (right boundary). In addition, the analytical solution is showed in the figure 3.2. It can observe a good agreement between analytical and numerical solutions. The only significant caution came from the selection of the geometry, a boundary condition away enough from the heating is recommended to avoid influence on results. Figure 3.3 shows the contours of temperature distribution along the axisymmetric geometry.

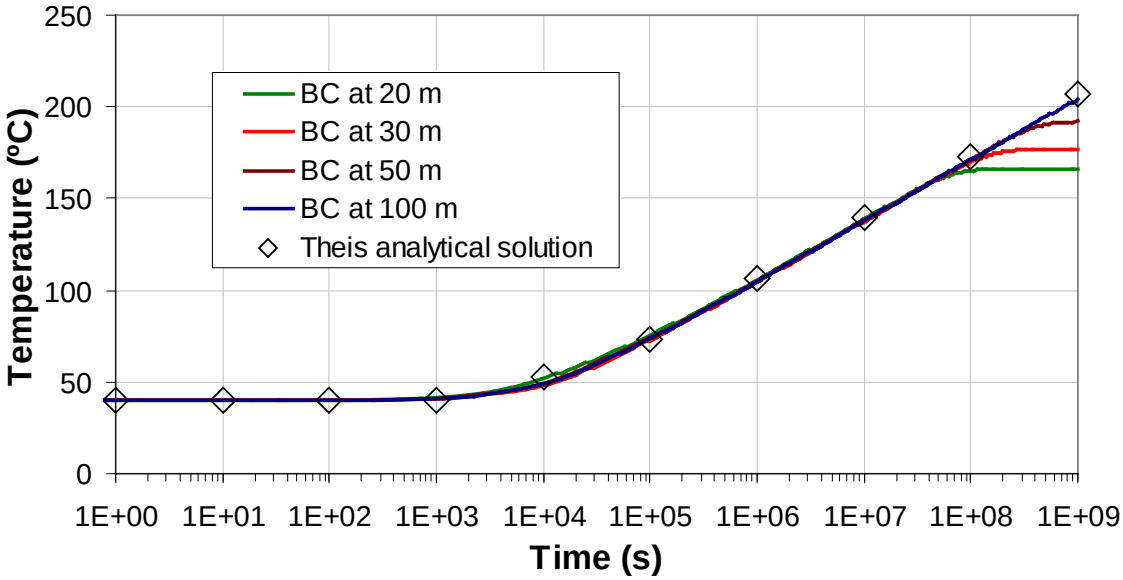

Figure 3.2 Variation of temperature in time, analytical and numerical predictions (Axisymmetric geometry)

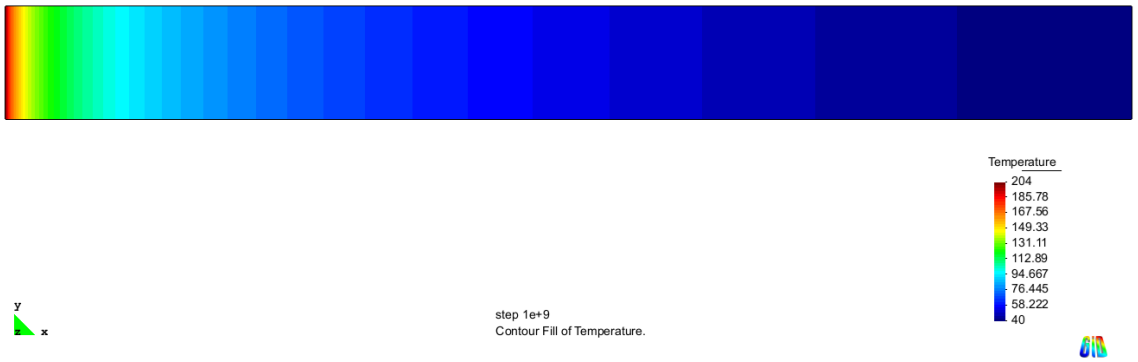

Figure 3.3 Contours of temperature distribution (Axisymmetric geometry)

3.2 Three-dimensional problem

The same problem is solved in three dimensions to verify that the same solution is obtained. Figure 3.4 shows the 3D geometry. A quarter of a cylindrical domain with a borehole is used taking advantage of symmetry of the problem. The same internal radius of r=0.25 m is considered and the external radius is set to b=25 m. Finite element mesh conformed by tetrahedral elements has been employed.

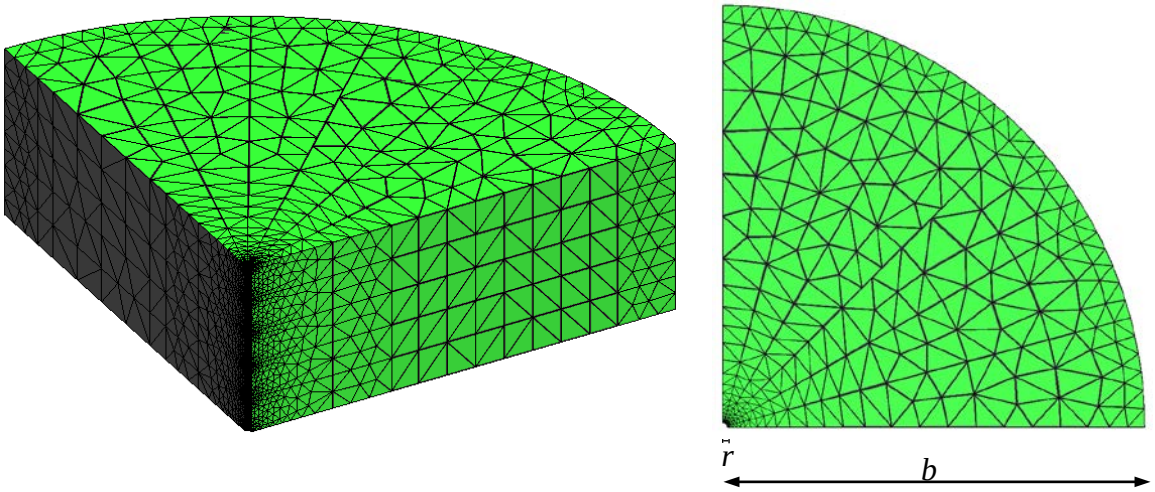

a) b)

Figure 3.4. 3D geometry and finite element mesh used. a) x-y-z plane. b) x-y plane

An initial temperature of T_o=40ºC is imposed on the external boundary (b=25m). A constant heat flow is imposed on the internal boundary. In the same way as in the Axisymmetric case, prescribed heat flow at the internal boundary (r=0.25m) per square meter or unit area is equal to $Q_{h\ applied} = Q_h / 2\pi rh = 592\ \mathrm{J/s/m^2}$, where h is the height of the cylindrical domain (h=10m). Note that the heat flux (heat flow per unit area) that is imposed in the axisymmetric case and in the three-dimensional case is exactly the same. Obviously, integration on the complete cylinder would give the total power per 10 m (9300 J/s) while integration on the quarter of cylinder would give a quarter of the power per 10 m (2325 J/s).

Results are shown in Figure 3.5, where it can be observed a good agreement between analytical and numerical solution. Again, an influence of the location of external boundary is observed. Figure 3.6 shows the contours of temperature distribution along the 3D geometry.

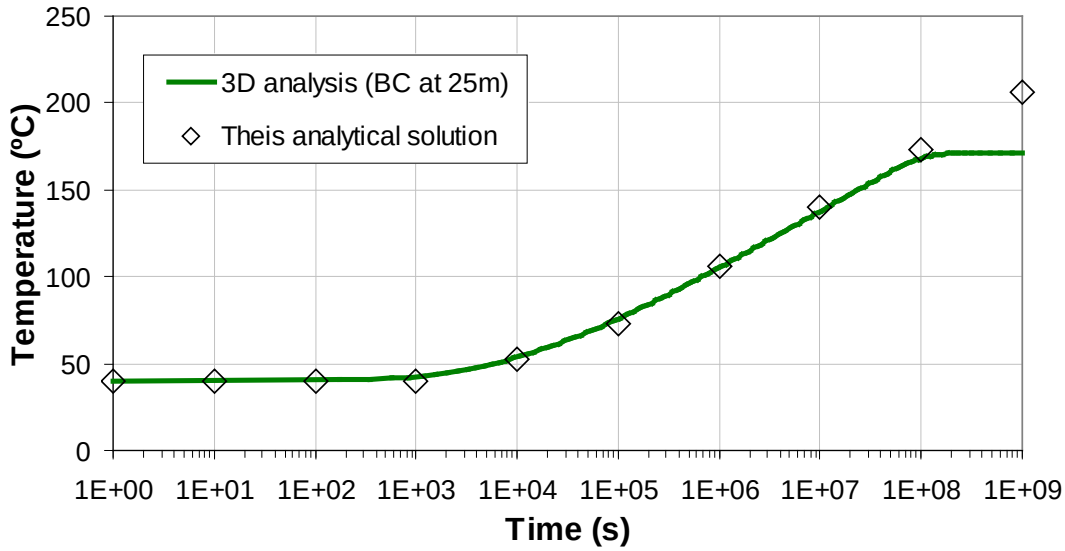

Figure 3.5 Variation of temperature in time, analytical and numerical predictions (3D geometry)

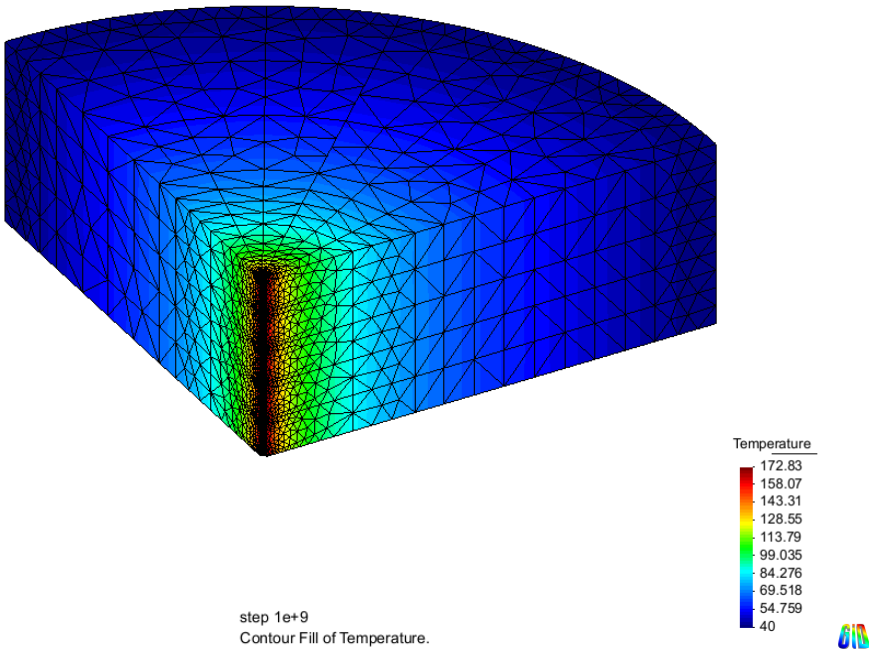

Figure 3.6. Contours of temperature distribution (3D geometry)

4 CONVERGENCE OF EXCAVATIONS

The convergence of excavations (long galleries, boreholes, large caverns or chambers) in salt formations is associated with the gradually decrease of volume excavation as time goes. The convergence is a result of both rock salt pressure and time dependent material behaviour (creep) and consequently strongly depends on depth and temperature.

Numerical solution of this problem is compared with the analytical solution used by Prij (1987). Analytical solution has been obtained using the following assumptions:

- The convergence of excavations is idealized as a thick-walled cylinder problem in a state of plane strain with a radial pressure (p).

- The constitutive behaviour of rock salt is described with a combination of elastic strains and secondary creep strains according to a Norton law,

$$\frac{\partial \varepsilon_{eq}^{cr}}{\partial t} = A(T)\sigma_{eq}^{n} \tag{4.1}$$

where,

ε_{eq}^{cr}, is the second invariant of the deviatoric strain tensor

$A(T)$, is a parameter depends on temperature

σ_{eq}^{n}, is the second invariant of the deviatoric stress tensor

n, is a power of the deviatoric stresses

- The creep strain components are calculated by a flow rule based on a normality principle,

$$\frac{\partial \boldsymbol{\varepsilon}^{cr}}{\partial t} = \frac{3}{2}\frac{1}{\sigma_{eq}}\frac{\partial \varepsilon_{eq}^{cr}}{\partial t}(\boldsymbol{\sigma} - p\boldsymbol{I}) \tag{4.2}$$

where,

$\boldsymbol{\varepsilon}^{cr}$, are the deviatoric components of the strain tensor

$\boldsymbol{\sigma} - p\boldsymbol{I}$, are the deviatoric components of the stress tensor

The analytical solution was derived introducing dimensionless variables allowing comparisons between convergence curves itself and with the analytical solution. The normalised radial creep displacement is calculated as,

$$\bar{u}(\tau) = \frac{u^{cr}(\tau, a)}{u^{el}(a)} \tag{4.3}$$

where,

$u^{cr}(\tau, a)$, are the total radial displacements at the cavity wall

$u^{el}(a)$, are the radial elastic displacements at the cavity wall

With the assumption of salt as incompressible medium, elastic displacements will be computed as,

$$u^{el}(a) = -\frac{3}{2}\frac{pa}{E} \tag{4.4}$$

Dimensionless time is defined as,

$$d\tau = EA\left(p\sqrt{3}\right)^{n-1} dt \tag{4.5}$$

where,

p , is the confining pressure

a , is the cavity radii

E , is the elastic moduli

The normalized convergence rate is written as,

$$k = \frac{du/dt}{du_{SS}/dt} \tag{4.6}$$

where,

du/dt , is the convergence rate at the cavity wall

du_{SS}/dt , is the stationary convergence rate at the cavity wall and the following analytical solution is used,

$$\frac{du_{SS}}{dt} = \frac{\sqrt{3}}{2} aA\left(\frac{p\sqrt{3}}{n}\right)^{n} \tag{4.7}$$

Convergence of an excavation with CODE_BRIGHT is simulated using an axisymmetric geometry with a radius of excavation a=0.25 m (Figure 4.1). As the radius of the excavation is much smaller than the thickness of the "salt wall" around it, the outer radius of the cylinder is considered very large and equal to b=25m (i.e. 100 times greater than a). The rock pressure p in the salt around the excavation was taken equal to p=-5 MPa.

Constitutive laws and parameters employed are listed in Table 4.1, the viscoplasticity model for saline materials was used. A constant temperature of T_0=40ºC was assumed to compute the parameter A in equation (4.1) as (see CODE_BRIGHT User's guide 2017):

$$A(T) = A_A \exp\left(\frac{-Q_A}{RT}\right) \tag{4.8}$$

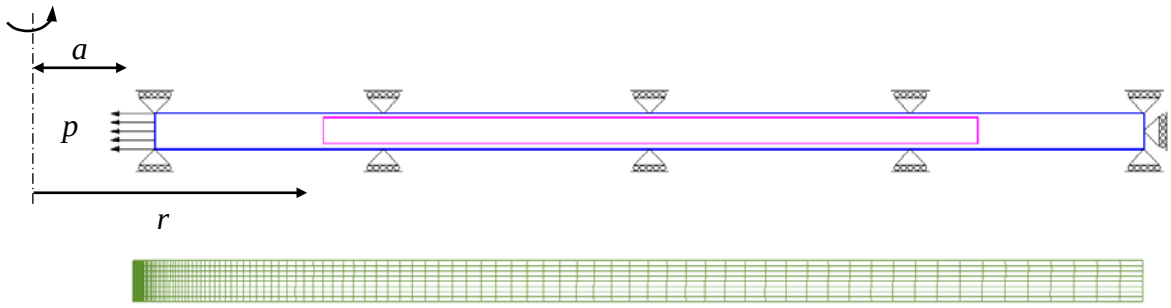

Figure 4.1 Geometry of and finite element mesh of a cylindrical cavity problem

MECHANICAL DATA	
Linear elasticity 1:	
ITYCL	1
P1: E (MPa)	25000
P3: ν	0.3
Viscoplasticity - creep:	
ITYCL	1
P1: A_A (s^{-1} MPa^{-n})	0.000005
P2: Q_A (J m^{-1})	60000
P3: n	2, 3, 4, 5, 5.5

Table 4.1 Constitutive laws and parameters for convergence excavation problem

The normalised total radial displacement computed with equation (4.3) against the normalised time computed with equation (4.5) is plotted in Figure 4.2. Total radial displacements at the cavity wall (U) are obtained from the numerical analysis using a creep exponent *n* of 5.5. Analytical solution (Prij, 1987) for *n=5.5* is also shown in Figure 4.2, for different values of *p*, *A* and *E*. It can be observed that numerical solution is close to the analytical solution when a Poisson's ratio near to 0.4 is selected.

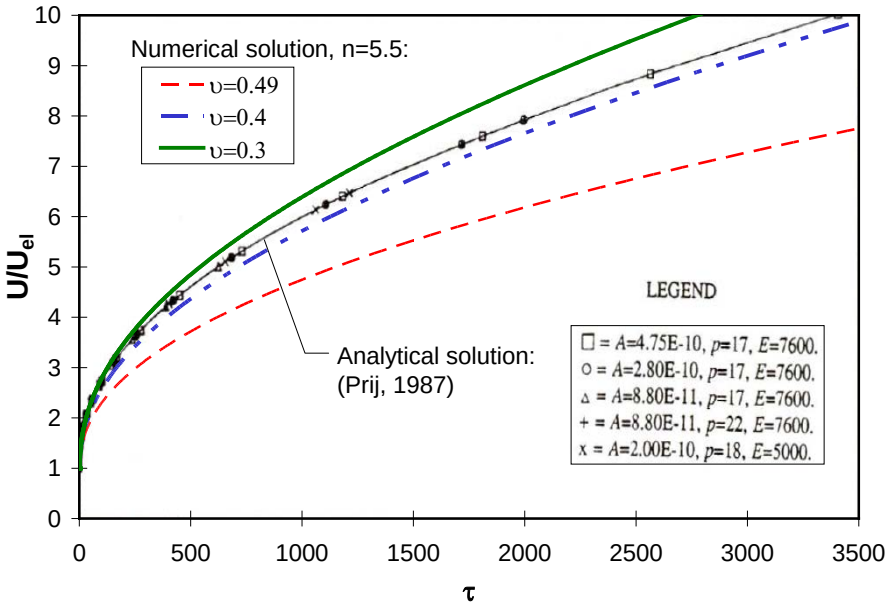

Figure 4.2. Normalised total radial displacement of a cylindrical cavity for *n*= 5.5. Comparison with analytical solution

A sensitivity analysis of the influence of *n* on the radial displacement at the cavity wall was done. Figure 4.3 shows the convergence curves for different *n* values in a double logarithmic scale of normalised radial displacement against normalised time. It is observed that smaller values of *n* induce larger total radial deformations.

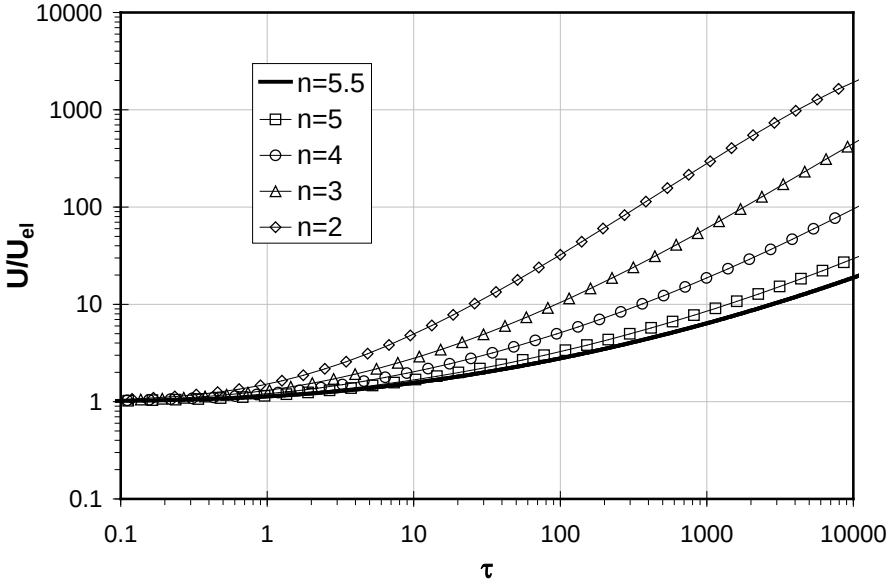

Figure 4.3. Normalised total radial displacement of a cylindrical cavity for different values of *n*

The normalized convergence rate (k) computed with equation (4.6) against the normalised time (equation 4.5) is plotted in Figure 4.4 for different values of n. The convergence rate, du/dt at the cavity wall, is obtained from the numerical analysis. Figure 4.4 shows that the convergence rate is strongly time dependent. Convergence rate increases for high values of n. It can be observed further that convergence rate does not reach a stationary value for n=2. This is supposed to be caused by numerical inaccuracies in the FEM solution for the large deformations.

For comparison proposes the normalised convergence rate obtained by Prij (1987) from his analytical solution is included in Figure 4.5. It will be observed some differences during the initial period between finite element results (Figure 4.4) an analytical results (Figure 4.5) for $n=5.0$ and $n=5.5$. Differences will be attributed to the fact that the finite element results represent the ratio of total radial deformation rate to stationary radial deformation rate while the analytical results give the ratio of radial creep deformation rate to stationary radial deformation rate, i.e., elastic deformations in analytical solution are ignored. Similar results are reported by Prij (1987) from his FEM analysis.

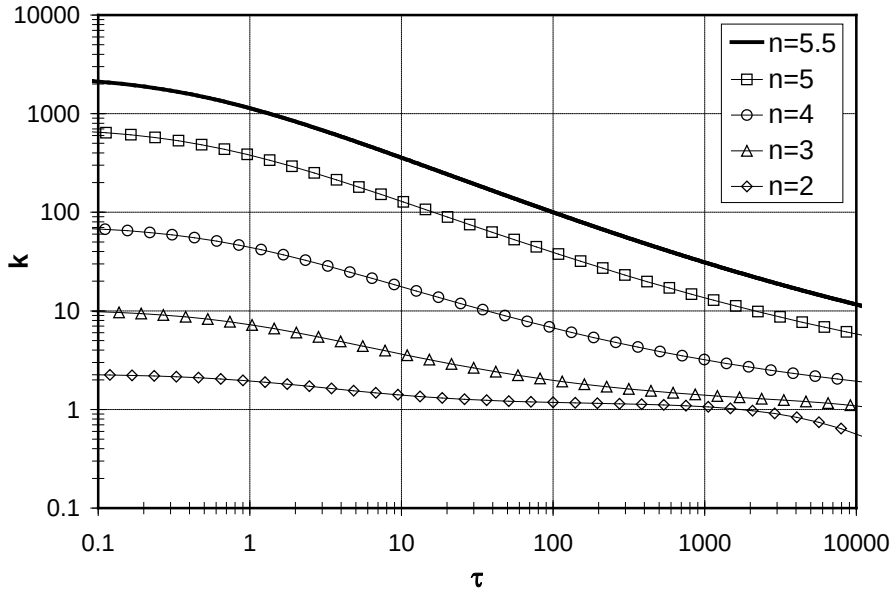

Figure 4.4. Normalised convergence rate of a cylindrical cavity for different values of *n*

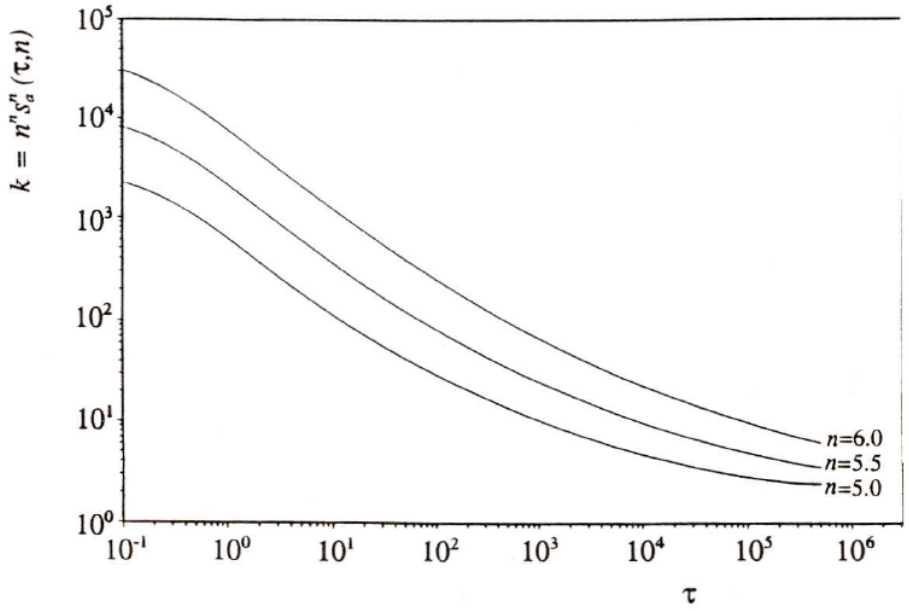

Figure 4.5. Analytical solution (from Prij, 1987) of normalised convergence rate of a cylindrical cavity for different values of *n*

The stress distribution is presented in Figure 4.6. Initial elastic stress is shown in Figure 4.6a), it is observed that radial stress (Sxx) at the cavity wall is twice hoop stress (Szz) and vertical stress (Syy) remains as zero, following elasticity. Stationary stress distribution is shown in Figure 4.5b). It is observed the enormous influence of creep induced stress redistribution (Sxx>Syy>Szz), this solution depends only on the creep exponent *n* and not on the other constitutive parameters. Figure 4.5 shows that for a relation r/a greater than 10 the initial elastic stress can be ignored but the stationary stresses are even significant for r/a > 20. The same results were given by Prij (1987).

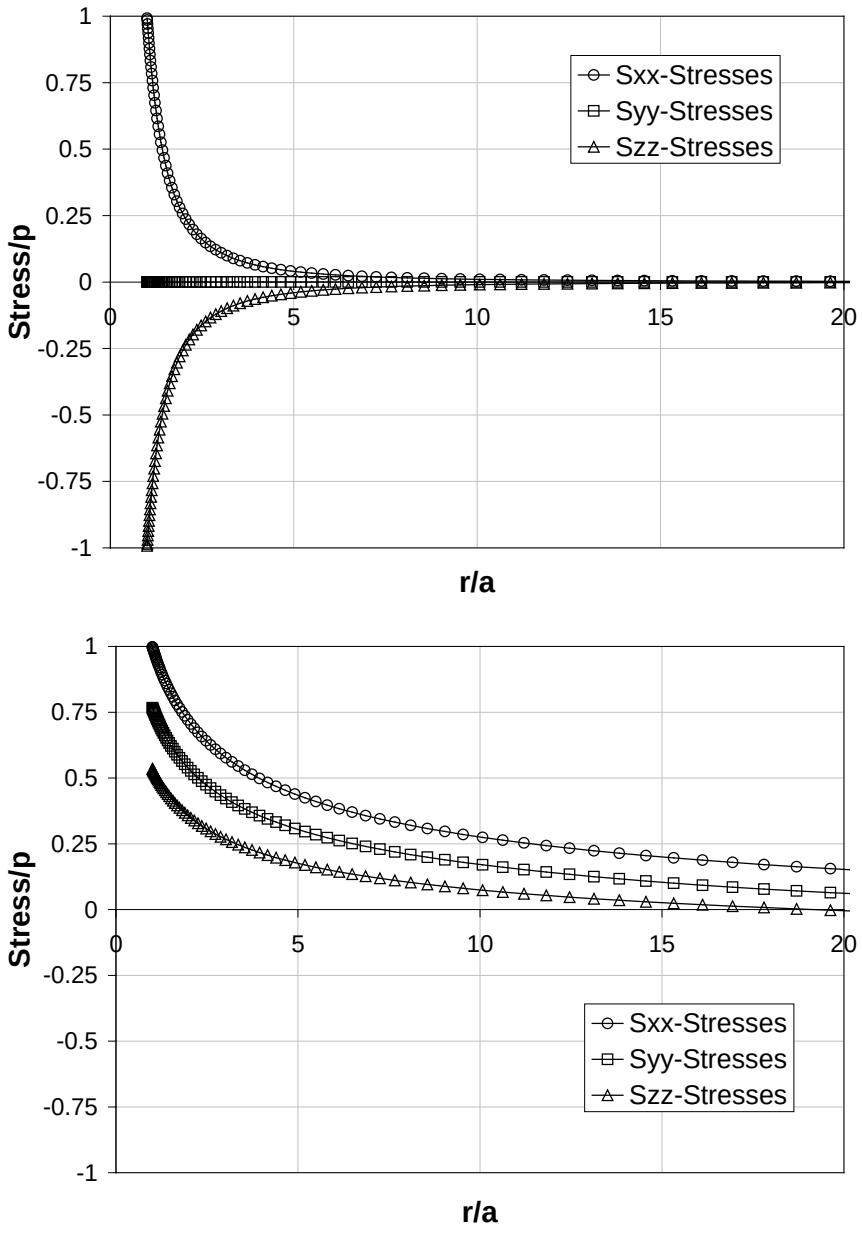

Figure 4.6. Normalised stress distribution of a cylindrical cavity for *n=5.5. a)* Initial (elastic) stresses b) Stationary stresses. (Sxx, Syy, Szz are radial, vertical and hoop stresses, respectively)

5 VERIFICATION OF MECHANICAL CONSTITUTIVE MODELS.

Code_bright considers some mechanical constitutive models that include the Barcelona Basic Model (BBM) law, this models are: Visco-plastic model (VP), Thermo-elasto-plastic model (TEP), Barcelona expansive model (BExM), damage-elastoplastic model for argillaceous rocks (Argillite), and Clay and sand model (CASM).

The following equations present the analytical solution of swelling strain, horizontal stress and swelling pressure of a material obeying the BBM elastic law:

Swelling strain

$$\varepsilon_y = \frac{(1+\upsilon)\kappa_s}{3(1+\upsilon)(1+e_0)} \ln\left(\frac{P_{atm}}{s_0 + P_{atm}}\right)$$

Horizontal stress:

$$\sigma_x = \frac{1}{2}\left[3\sigma_{z0}\left(\frac{P_{atm}}{s_0 + P_{atm}}\right)^{\frac{2\kappa_s}{3\kappa}\frac{1-2\upsilon}{1-\upsilon}} - \sigma_{z0}\right]$$

Swelling pressure:

$$\sigma_y = \sigma_{y0}\left(\frac{P_{atm}}{s_0 + P_{atm}}\right)^{\frac{\kappa_s}{\kappa}}$$

A simulation of an oedometer test, involving load at constant suction, wetting at constant vertical stress and loading under saturated conditions, was used in order to evaluate the response of the different constitutive models. The results were compared with the analytical solution. Table 5.1 presents the parameters employed in the simulation for all the constitutive models consider.

Termo elasto-plastic (TEP)	
ICL=21: Elastic parameters	
ITYCL	1
P1: κ_{i0}	0.01
P2: κ_{s0}	0
P3: K_{min} *(MPa)*	0.1
P5: υ	0.35
ICL=23: Plastic parameters (1)	
ITYCL	1
P1: $\lambda(0)$	0.135
P2: r	0.75
P3: β *(MPa^{-1})*	35
P5: k	0
P6: p_{s0} *(MPa)*	0

Visco plastic model (VP)	
ICL=4: Nonlinear Elasticity	
ITYCL	1
P1: $-\kappa/(1+e)$	-0.0055
P2: $-\kappa_s/(1+e)$	0
P5: ν	0.35
P6: *tens (MPa)*	0
P7: K_{min} *(MPa)*	0.1
ICL=34: VPUSR 1	
ITYCL	1
P1: Γ_o *(1/s)*	100
P2: N	3
P3: F_o *(MPa)*	1
P5: b	1

ICL=24: Plastic parameters (2)	
ITYCL	1
P1: p^c *(MPa)*	0.01
P2: M	1.07
P3: α	1
P4: e_0	0.825
P5: p_0^* *(MPa)*	0.06
ICL=25: Shape yield surface	
ITYCL	3
ICL=26: Shape plastic potential	
ITYCL	3
ICL=27: Integration control parameters	
ITYCL	1
P1: *Tole1*	1.E-8
P2: *Tole2*	1.E-3
P3: *Tole2*	1.E-3
P4: μ	1
P5: *Index*	-1

ICL=35: VPUSR 2	
ITYCL	1
P1: n	1
P2: γ	-0.111
P5: μ_{DRY}	1.07
P7: $(J_1^{o*})_F$ *(MPa)*	0.18
P8: $(J_1^{o*})_G$ *(MPa)*	0.18
P9: a	3
P10: μ_{SAT}	1.07
ICL=36: VPUSR 3	
ITYCL	1
P1: κ	0.01
P2: $\lambda(0)$	0.135
P3: r	0.75
P4: β *(MPa^{-1})*	35
P5: p^c *(MPa)*	0.01
P7: k_2	0
P8 k_3	0

Argillite	
ICL=71: Argillite matrix	
ITYCL	3
P1: κ^M	0.0055
P2: ν^M	0.35
P3: κ_s^M	0
ICL=72: Coupling behaviour	
ITYCL	1
P1: χ_0	0
ICL=73: BBM (YS shape in p'-q)	
ITYCL	3
P1: M^M	1.07
P3: r^M	0.75
P4: β^M*(MPa^{-1})*	35
P5: p^{cM}*(MPa)*	0.01
P6: k_s^M	0
ICL=74: BBM (YS shape in deviatoric plane)	
ITYCL	3
P1: θ_t^M *(°)*	25
ICL=75: BBM (plastic potential shape in p'-q)	
ITYCL	3
P1: ω^M	1
ICL=77: BBM hardening law	
ITYCL	3
P1: $\lambda^M(0)$	0.135
ICL=79: Control parameters	
ITYCL	1
P1: *tol*	1e-8
P2: *itmax*	30
P3: *isubmax*	500
P4: *iJac*	-1

BExM model	
ICL=81: Elastic model	
ITYCL	1
P1: κ^{Macro}	0.0055
P2: κ^{Micro}	1e-10
P5: κ_s^{Macro}	0
P6: ν^M	0.35
P7: K_{min}^{Macro}*(MPa)*	0.1
P8: K_{min}^{Micro}*(MPa)*	0.1
ICL=82: Coupling behaviour	
ITYCL	1
P1: χ_0	0
ICL=83: BBM (YS shape in p'-q)	
ITYCL	1
P1: M	1.07
P3: r	0.75
P4: β*(MPa^{-1})*	35
P5: p^c*(MPa)*	0.01
P6: k_s	0
P6: p_{t0} *(MPa)*	0
ICL=85: BBM (Plastic potential in p'-q)	
ITYCL	1
P1: ω	1
ICL=87: BBM hardening law	
ITYCL	1
P1: $\lambda(0)$	0.135
ICL=88: Control parameters	
ITYCL	1
P1: *tol*	1e-8
P4: *toler_ini_SI_SD*	Fixed as initial conditions γ_{SI}=1e6 γ_{SD} = -1e6

CASM	
ICL=90: CASM saturated parameters	
ITYCL	2
P1: ν	0.35
P2: κ	0.01
P3: $\lambda(0)$	0.135
P4: r	2
P5: n	1.5
P6: M	1.07
ICL=91: CASM Unsaturated parameters	
ITYCL	2
P1: P_r *(MPa)*	0.01
P2: r^*	0.75
P3: β*(MPa^{-1})*	35
P4: κ_s	0
P5: k_s	0
P6: iunsat	0 : Net stress

Table 5.1 Parameters employed for oedometer test simulation realized with different mechanical constitutive models.

Figure 5.1 presents a comparison of the simulation carried out with the different constitutive models and the analytical solution in the plane void ratio vs mean effective stress. In figure 5.2 can be appreciate a comparison of all the constitutive models in the plane Ko vs mean effective stress. In both figures can be seen that the solutions obtain with all the constitutive models are very close and correspond with the values for the analytical solution.

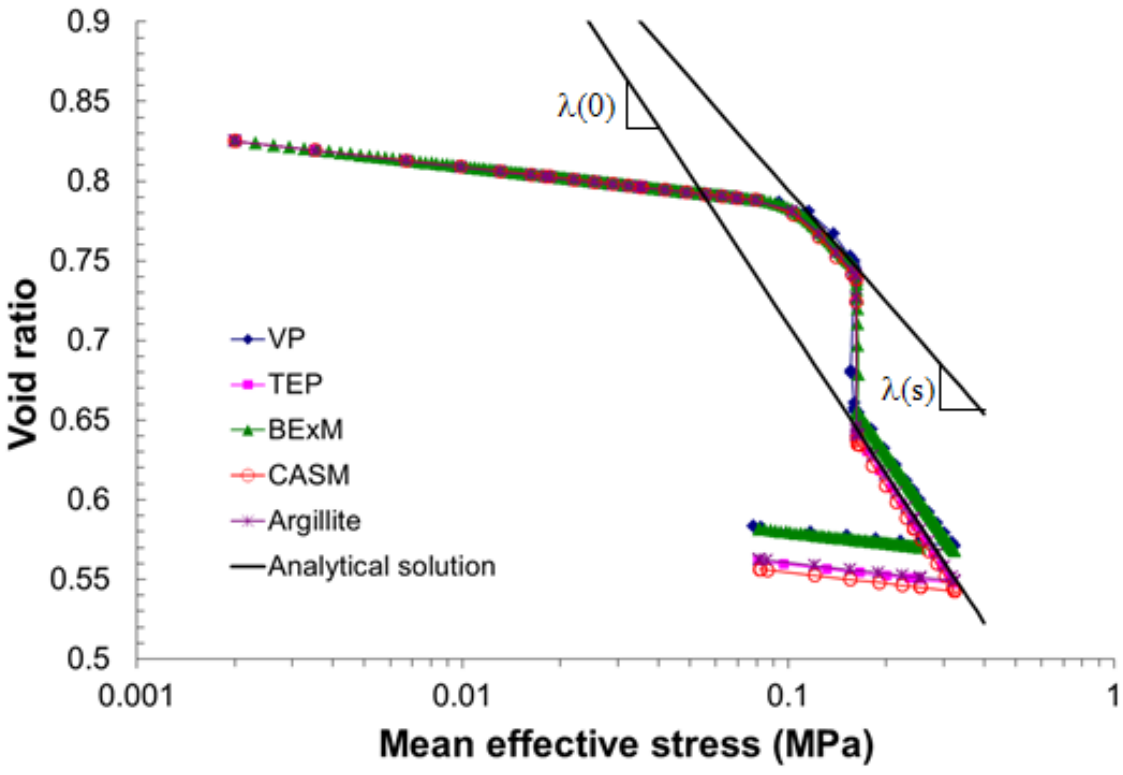

Figure 5.1 Comparison in void ratio vs mean effective stress plane

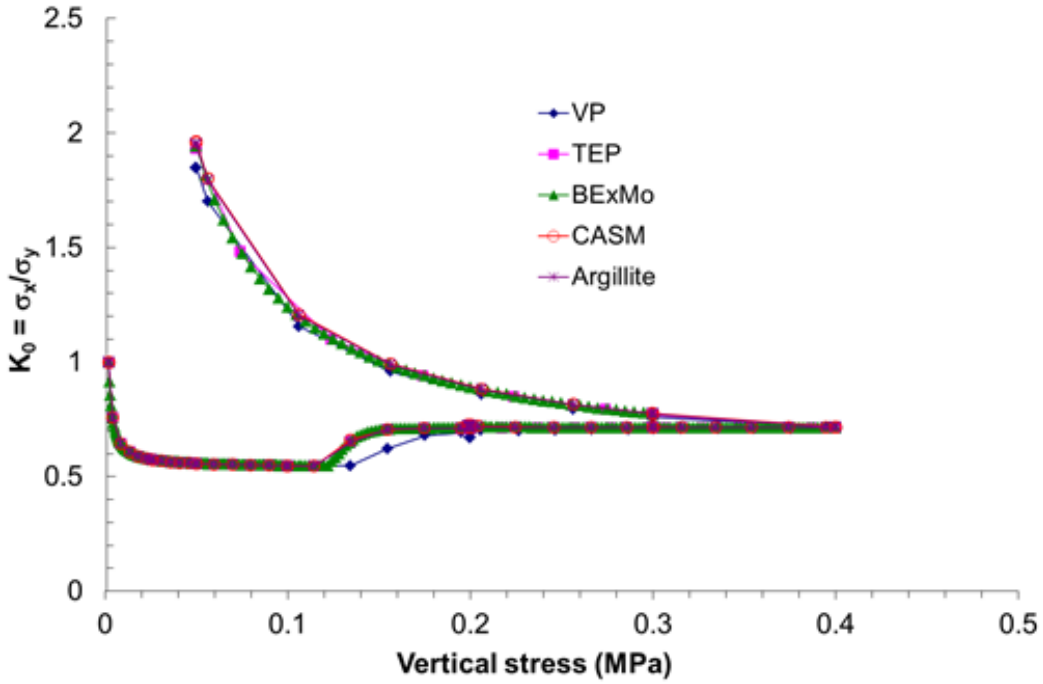

Figure 5.2 Comparison in K0 vs mean effective stress plane

REFERENCES

CODE_BRIGHT User's Guide (2018). Civil and Environmental Engineering Department, Technical University of Catalunya, Spain (digital format available at https://deca.upc.edu/en/projects/code_bright).

Prij, J.(1987). On the design of a radioactive waste repository. PhD thesis. University of Twente, Netherlands.

Theis, C.V. (1935). The relation between the lowering of the piezometric surface and the rate and duration of discharge of a well using groundwater storage, Am. Geophys. Union Trans., vol. 16, pp. 519-524.